# Strain Control of Phase Transition and Magnetic Property in Multiferroic $BiFeO_3$ Thin Films

Wanchao Zheng ConceptualizationMethodologyValidationInvestigationResourcesFormal analysisWriting - Original
Dongxing Zheng InvestigationWriting - Original DraftFunding acquisition ,
Dong Li InvestigationWriting - Review & Editing ,
Peng Li InvestigationWriting - Review & Editing ,
Linxing Zhang InvestigationWriting - Review & Editing ,
Junlu Gong Writing - Review & Editing ,
Xin Pang Writing - Review & Editing ,
Chao Jin Writing - Original Draft ,
Xixiang Zhang Writing - Review & EditingFunding acquisition ,
Haili Bai Writing - Original DraftFunding acquisition

PII: S0040-6090(19)30766-7
DOI: https://doi.org/10.1016/j.tsf.2019.137741
Reference: TSF 137741

To appear in: *Thin Solid Films*

Received date: 4 October 2019
Revised date: 21 November 2019
Accepted date: 8 December 2019

Please cite this article as: Wanchao Zheng ConceptualizationMethodologyValidationInvestigationResourcesFormal Dongxing Zheng InvestigationWriting - Original DraftFunding acquisition , Dong Li InvestigationWriting - Review & Peng Li InvestigationWriting - Review & Editing , Linxing Zhang InvestigationWriting - Review & Editing , Junlu Gong Writing - Review & Editing , Xin Pang Writing - Review & Editing , Chao Jin Writing - Original Draft , Xixiang Zhang Writing - Review & EditingFunding acquisition , Haili Bai Writing - Original DraftFunding acquisition , Strain Control of Phase Transition and Magnetic Property in Multiferroic $BiFeO_3$ Thin Films, *Thin Solid Films* (2019), doi: https://doi.org/10.1016/j.tsf.2019.137741

HIGHLIGHTS

- The high quality $BiFeO_3$ thin films were prepared by magnetron sputtering.
- In the 17-nm-thick $BiFeO_3$ thin films, an obvious magnetic moment is induced by spin canting.
- The orbital reconstruction exists at the mixed BFO phase boundaries.

*Manuscript to Thin Solid Films*

# Strain Control of Phase Transition and Magnetic Property in Multiferroic $BiFeO_3$ Thin Films

Wanchao Zheng[1], Dongxing Zheng[1], Dong Li[1], Peng Li[2], Linxing Zhang[3], Junlu Gong[1], Xin Pang[1], Chao Jin[1], Xixiang Zhang[2], and Haili Bai[1,*]

[1]*Tianjin Key Laboratory of Low Dimensional Materials Physics and Processing Technology, School of Science, Tianjin University, Tianjin 300350, People's Republic of China*

[2]*King Abdullah University of Science & Technology (KAUST), Physical Science and Engineering (PSE) Division, Thuwal 23955-6900, Saudi Arabia*

[3]*Institute of Advanced Materials and Technology, University of Science and Technology Beijing, Beijing 100083, People's Republic of China*



* Author to whom all correspondence should be addressed.

E-mail: baihaili@tju.edu.cn

# Abstract

$BiFeO_3$ (BFO), a room-temperature antiferromagnetic-ferroelectric multiferroic, is widely researched due to its potential applications for electric-field control of the magnetism. In this work, the strain control of the phase transition and magnetic properties in the BFO/$LaAlO_3$ heterostructures were investigated. The O *K* edge polarization-dependent X-ray absorption spectroscopy (XAS) spectra show that the Fe 3*d* level splits into five levels, which proves that the $FeO_5$ pyramid is asymmetric in the highly strained tetragonal-like BFO. The spin canting induced by the asymmetric structure leads to the magnetic moment. Thus, an obvious magnetic signal in the 17-nm-thick BFO thin films was observed by the Quantum Design magnetic property measurement system. With the increase of the BFO film thickness, the clamping effect induced by the substrate becomes weak, further leading to the BFO phase transition. The O *K* edge polarization-dependent XAS spectra demonstrate that the orbital reconstruction exists at the mixed BFO phase boundaries. Since the orbital reconstructions can induce the strong magnetic coupling, the magnetic order of the different BFO phases will be coupled with each other. It causes a variation of the magnetic property at the phase boundaries or in the BFO phases.

**Keywords:** Strain effect; Spin canting; Orbital reconstruction; Magnetic moment; Bismuth ferrite

**PACS numbers:** 68.35.Gy; 75.70.Tj; 75.25.Dk; 07.55.Jg; 77.55.Nv

## 1. Introduction

Multiferroics simultaneously possess varieties of ferroics, such as ferromagnetism, ferroelectricity and ferroelasticity [1, 2]. Apart from their intriguing properties, multiferroics could be applied in numerous fields, such as optoelectronics, spintronics and agile electromagnetics [3, 4]. The magnetoelectric coupling in multiferroics provides a chance to reverse magnetization by applying an electric field instead of a magnetic field, which would benefit the design of next generation information storage technology with fast speed and low energy cost [2, 5, 6]. $BiFeO_3$ (BFO) is the single phase multiferroics with coexisted room-temperature ferroelectricity (the Curie temperature $T_C$ =1103 K) and antiferromagnetism (the Néel temperature $T_N$=643 K), which has attracted wide attentions [7, 8]. Through strain engineering, various phases such as rhombohedral bulk-like (*R*-), tetragonal-like (*T*-), and orthorhombic phases, can be attained in the BFO thin films, which show completely different magnetic properties and polarization vectors (*P*) [9–17]. With the different epitaxial strains, the BFO thin films can show different antiferromagnetic orders. With the lower compressive strain, the bulk-like cycloidal spin modulation exists in the BFO thin films, and with the higher strain (both compressive and tensile), the pseudo-collinear antiferromagnetism appears in the BFO thin films [18]. The $P_{R\text{-BFO}}$ in the *R*-BFO is ~90–120 μC/cm$^2$ along the $[111]_{pc}$ direction, and the $P_{T\text{-BFO}}$ in the *T*-BFO is ~150 μC/cm$^2$ along the $[001]_{pc}$ direction [19–21]. In the BFO/$LaAlO_3$ (LAO), the structure of the BFO changes as the film thickness increases. However, the corresponding magnetic property in the *T*-BFO thin films has been rarely reported.

In this work, we investigate the strain modulation of the BFO phases and the magnetic property in the *T*-BFO thin films with various thicknesses. The polarization-dependent X-ray absorption spectroscopy (XAS) spectra demonstrate that the $FeO_5$ pyramid structure in the highly strained *T*-BFO is asymmetric, which induces the spin canting and further leads to the magnetic moment. With the increase of the film thickness, the orbital reconstruction between different BFO phases was observed by the polarization-dependent XAS spectra, which causes the variation of the magnetic order at the BFO phase boundaries or in the BFO phases.

## 2. Experimental details

The BFO thin films were fabricated on the LAO (001) substrates by radio-frequency magnetron sputtering. The deposition temperature, the sputtering power and the gas pressure were 650 °C, 40 W and 1.2 $kg*m^{-1}*s^{-2}$, respectively. The flow ratio of the Ar and the $O_2$ is 5/4. The BFO thin films with different thicknesses were acquired by changing the sputtering time. The sputtering time was 20, 50, 100, 150, 200 min and the deposition ratio was 0.85 nm/min. To avoid the volatilization of the Bi element and the appearance of the $Fe^{2+}$ in the BFO, the BFO thin films were prepared by a $Bi_{1.1}FeO_3$ target and were cooled down to room temperature in pure $O_2$ atmosphere at 200 $kg*m^{-1}*s^{-2}$. The thicknesses of the BFO layer were measured by the Dektak 6M surface profiler. The crystal structure was analyzed by X-ray diffraction (XRD) (Cu *K*α radiation, $\lambda$=1.54056 Å, and Beijing Synchrotron Radiation Facility, beamline 1W1A, $\lambda$=1.5491 Å), reciprocal space map (RSM, Beijing

Synchrotron Radiation Facility, beamline 1W1A) and transmission electron microscopy (TEM). The TEM apparatus model is the Tecnai G2 F20 S-Twin. During the process of the sample preparation, the sample was divided into two parts and stuck face to face by the M-Bond 610. Then, the sample was grinded by the mechanical thinning method. When the sample thickness along the normal of the cross section was below 20 μm, the sample continued to be thinned by the Gatan691 Precision Ion Polishing System. The thinning process was finished until the canting angle (the angle between the cross section and the BFO thin film surface) changed from 10° to 4°. Finally, the sample was observed by the TEM and the acceleration voltage of the electronic gun was 200 kV. Surface morphologies were imaged by the Bruker Multimode 8 atomic force microscopy (AFM). XAS spectra were performed at beamline 4B9B of the Beijing Synchrotron Radiation Facility. Polarization-dependent XAS spectra were acquired by recording the surface sensitive total electron yield current as a function of X-ray photon energy at beamline 12B-a of the National Synchrotron Radiation Laboratory in Hefei, China. Hysteresis loops (*M–H*), thickness dependent magnetization (*M–t*) and temperature dependent magnetization (*M–T*) were measured using a Quantum Design magnetic property measurement system (Superconducting Quantum Interference Device, SQUID). The *M–T* curves were measured after zero field cooling (ZFC) and field cooling (FC) under 0.03 T. X-ray magnetic circular dichroism (XMCD) spectra were carried out at beamline 08U1A of Shanghai Synchrotron Radiation Facility. The measurements were done under high vacuum ($6.7\times10^{-7}$ $kg*m^{-1}*s^{-2}$) at room temperature. The direction of the external

magnetic field and the incident beam was perpendicular to the surface of the samples.

## 3. Results and discussion

### *3.1 Structural characterization*

Figure 1(a) shows the XRD patterns of the LAO substrate and the BFO thin films with film thickness varying from 17 to 170 nm. In the XRD pattern of the 17-nm-thick BFO thin films, only the *T*-BFO (001), (002), (003) and (004) peaks which are located at the 19.3°, 38.98°, 60.22° and 83.16° appear [22, 23], expect for the diffraction peaks from the LAO substrate. It suggests that the BFO thin films grow on the LAO substrate with a (001) orientation and indicates that the high strain from the substrate is applied on the BFO thin film [24]. With the increasing thickness, the compressive strain driven by the LAO substrate gradually relaxes. In the XRD pattern of the 85-nm-thick BFO thin films, the (001) diffraction peak of the $S'_{tilt}$ phase ($c$~0.42±0.03 nm) is observed [25, 26], implying the coexistence of the *T*-BFO and the $S'_{tilt}$ phases. In the XRD pattern of the 170-nm-thick BFO thin films, the *R*-BFO (001), (002) and (003) peaks which are located at the 22.56°, 45.84°, and 71.36° appear [22, 24], demonstrating the existence of the *R*-BFO phase. These results reveal that the *T*-BFO phase transforms into the other BFO phases (including intermediate monoclinic ($S'_{tilt}$) and *R*-BFO phases) as the film thickness increases and all the BFO phases have a (001) orientation.

To gain further insights into the structure of the BFO, RSM patterns of the (103) diffraction condition were performed, as shown in Figs. 1(b) to 1(d). Figure 1(b)

shows four peaks, which correspond to the (103) diffraction peaks of the LAO substrate and the *T*-BFO. In the RSM measurement, since the reference plane is the LAO (103) plane, the peak at the *H*=1, *L*=3 is the (103) diffraction peaks of the LAO substrate. Due to the $c_{\mathrm{LAO}}$~0.3789 nm and $c_{T\text{-BFO}}$~0.4655 nm [25], the peaks around the *H*=0.99, *L*=2.5 is the (103) diffraction peaks of the *T*-BFO. In Fig. 1(b), one peak shifts upward and another peak shifts downward with respect to the central peak. It demonstrates that the structure of the *T*-BFO is distorted with a small angle tilting along the [100] orientation. The monoclinic angle $\beta$ extracted from the (103) RSM is 88.9°±0.3°, more than the reported value 88.12° [24, 25]. It demonstrates that the high compressive strain is applied to the *T*-BFO in the 17-nm-thick BFO thin films. The overlapping of the (013) and the $(0\bar{1}3)$ peaks reflects that the *a*-axis is perpendicular to the *b*-axis. According to the RSM patterns, the lattice constants of the *T*-BFO were calculated as shown in the Tab. 1. These results confirm that the *T*-BFO in the 17-nm-thick BFO thin films is the highly strained *T*-BFO. With the increase of the thickness, the *c*-axis lattice constants of the *T*-BFO increase and then almost remain unchanged. In the 170-nm-thick BFO thin films, the lattice constants are consistent with that of the previous reports [22, 24, 25, 27–29]. The monoclinic angles $\beta$ extracted from the (103) RSM are 88.5°±0.3° in the 85-nm-thick BFO thin films and 88.0°±0.3° in the 170-nm-thick BFO thin films, respectively. The varied lattice constants and the decreased $\beta$ indicate the transformation from the highly strained *T*-BFO to the *T*-BFO and the relaxation of the compressive strain. In Fig. 1(c), two diffraction peaks appear at the *H*=0.955, *L*=2.465 and *H*=1.07, *L*=2.41. It reveals that

the diffraction peaks are the (103) diffraction peaks of the $M_{C,tilt}$ [25]. With the increase of the film thickness, the diffraction peak of the $S'_{tilt}$ at the $H$=1.095, $L$=2.67 emerges in Fig. 1(d) [25, 30]. According to the XRD and RSM patterns, the highly strained $T$-BFO→$T$-BFO→$M_{C,tilt}$→$S'_{tilt}$→$R$-BFO phases transition occurs with the increase of the film thickness.

To reflect the quality of the BFO thin films and the relationship between the BFO phases and the thickness, the surface morphologies of the BFO thin films were obtained by AFM. In Fig. 2(a), the atomically smooth morphology of the 17-nm-thick BFO thin films is observed with the step height ($\Delta h$~0.92±0.03 nm) of nearly two unit cell as a result from the superposition of the atomic layer. With the increasing thickness of the BFO thin film, a striped contrast gradually emerges due to the different $c$-axis lattice parameters of various BFO phases [23], as shown in Figs. 2(b)–(d). The bright plateau areas comprise the $T$-BFO and the $M_{C,tilt}$ phases while the dark banded needle-like structures consist of the $R$-BFO and the $S'_{tilt}$ phases. It reflects that the $S'_{tilt}$ or the $R$-BFO or both phases exist in the 43-, 85- and 170-nm-thick BFO thin films. However, there are no (00$l$) peaks of the $R$-BFO in the XRD pattern of the 85-nm-thick BFO thin films, suggesting that the dark banded needle-like structures in the 43- and 85-nm-thick BFO thin films represent the $S'_{tilt}$. Due to the existence of the $R$-BFO and the $S'_{tilt}$ peaks in the XRD pattern of the 170-nm-thick BFO thin films, the dark banded needle-like structures in the 170-nm-thick BFO thin films represent the $R$-BFO and the $S'_{tilt}$. These results reveal the high quality of the BFO thin films, and the transformation of the $T$-BFO phase to

the other phases (including the *R*-BFO, the $S'_{tilt}$ and the $M_{C,tilt}$) with the relaxation of the compressive strain.

To analyze the quality and the in-plane structure of the highly strained *T*-BFO, TEM patterns of the 17-nm-thick BFO thin films were performed, as shown in Fig. 3. The cross-sectional image in Fig. 3(a) confirms the thickness of the BFO thin films. Figures 3(b) and (c) present the high resolution TEM (HRTEM) images of the BFO/LAO interfaces. In Fig. 3(b), some local interface defects are observed at the BFO/LAO interface. Moreover, the positions of the Fe ion in BFO unit cells are different for the region A and B. In order to clearly demonstrate this phenomenon, the magnified images are shown in Figs. 3(d) and (e). In Fig. 3(d), the Fe ions in the left part of the image are located at the upper-left of the BFO unit cell, but the Fe ions in the right part of the image are located at the upper-inward (or upper-outward) part of the BFO unit cell. Similarly, in Fig. 3(e), the Fe ions in the right part of the image are located at the upper-right of the BFO unit cell, but the Fe ions in the left part of the image are located at the upper-inward (or upper-outward) part of the BFO unit cell. This phenomenon is related to the highly strained *T*-BFO structure. Since the lattice constants $a$~0.382±0.002 nm and $b$~0.379±0.002 nm of the highly strained *T*-BFO are different and the in-plane structure of the LAO is isotropic, both the [100] and [010] orientations of the BFO can be parallel to the [100] orientation of the LAO. And it demonstrates the in-plane structure disorder in the 17-nm-thick BFO thin films. Moreover, since the O ions in the BFO unit cell are located at face-centered position, the positions of the O ions can be deduced according to the positions of the Bi ions. In

Figs. 3(d) and (e), the Fe ions are located at the off-centered position, indicating that the Fe ions deviate from the center of the $FeO_5$ pyramid.

## *3.2 X-ray absorption spectroscopy spectra*

In order to further analyze the quality of the BFO thin films and the BFO structure, the Fe $L_{2,3}$ edge XAS spectra were performed, as shown in Fig. 4. In Fig. 4(a), the peaks in the Fe $L_{2,3}$ edge XAS spectra occur around 708.4, 709.4, 721.6 and 723 eV, demonstrating that the Fe valence state is +3 [31]. In the highly strained *T*-BFO, the *T*-BFO and the $M_{C,tilt}$, the Fe ions are in square pyramidal sites. In the $S'_{tilt}$ and the *R*-BFO, the Fe ions are in the octahedral sites. In the $\gamma$-$Fe_2O_3$, the Fe valence is also +3, and five of the eight Fe ions are in octahedral sites while the others are in tetrahedral sites [32]. Thus, the 723 eV peak shapes of the Fe $L_2$ edge XAS spectra for the *T*-BFO and the $\gamma$-$Fe_2O_3$ are different. Figure 4(b) shows the XAS spectra of the Fe $L_2$ edge for the BFO thin films. Obviously, for the 17-nm-thick BFO thin films, the 723 eV peak shape of the Fe $L_2$ edge is distinctly different from that of the BFO samples with the $\gamma$-$Fe_2O_3$ impurity [33]. It reveals the inexistence of the $\gamma$-$Fe_2O_3$. These results further confirm that only the BFO phases exist in the BFO thin films without the impurity phases. With the increase of the thickness, the 723 eV peak shapes of the Fe $L_2$ edge change. Since the measurement depth of the XAS is only several nanometers, the XAS is not deep enough to detect the orbital information of the inner layers. With the increase of the film thickness, the highly strained *T*-BFO phase transforms into the other phases (such as the *R*-BFO, the $S'_{tilt}$, the $M_{C,tilt}$ and the

*T*-BFO). Thus, as the film thickness increases, the XAS spectra of different BFO phases overlap, causing the variation of the line shape in the XAS spectra.

As the Fe ions are surrounded by O ions in the BFO, the site of the Fe ions can be determined by the polarization-dependent O *K* edge XAS spectra. Figure 5 shows the 3*d* level splits for different site symmetries and the polarization-dependent O *K* edge XAS spectra. In Fig. 5(a), the 3*d* level of single Fe ion is fivefold degenerated, according to the ligand field theory. In octahedral symmetry, the fivefold degenerated 3*d* level splits into two levels of doublet $e_g$ and triplet $t_{2g}$. Although the oxygen octahedron slightly tilts in the *R*-BFO, the orbital anisotropy is minimal and the fivefold degenerated 3*d* level still splits into two levels [34]. When the oxygen octahedron is elongated along the *c*-axis, the oxygen octahedron transforms into the $FeO_5$ pyramid. And it can cause the Jahn-Teller-type level splitting [35]. In the *T*-BFO, the formation of the $FeO_5$ pyramid is induced by the displacement of the Fe ions along the *c*-axis. According to the RSM and TEM patterns of the 17-nm-thick BFO thin films, the structure of the highly strained *T*-BFO is distorted with a small angle tilting along the <100> orientation, which will lead to the distortion of the $FeO_5$ pyramid. Further, the Fe ions shift to the upper-right of the $FeO_5$ pyramid, leading to the elongation of the in-plane Fe-O bond length and the shrinkage of the out-of-plane Fe-O bond length. The fivefold degenerated 3*d* level splits into five levels in the highly strained *T*-BFO. Figure 5(b) shows the polarization-dependent O *K* edge XAS spectra for the 17-nm-thick BFO thin films. The different spectra with the different incoming light polarizations (*E*//*c* and *E*//*a*) indicate the strong orbital anisotropic.

Based on the strict dipole selecting rules in polarization-dependent XAS spectra, the *E*//*c* incoming light enhances the absorption to the O 2*p* states hybridized with the out-of-plane orbitals ($d_{yz}$, $d_{zx}$ and $d_{3z^2-r^2}$) while the *E*//*a* incoming light enhances the absorption to the O 2*p* states hybridized with the in-plane orbitals ($d_{xy}$ and $d_{x^2-y^2}$) [34]. By comparing with the slope of the O *K* edge XAS spectra with the *E*//*a* and the *E*//*c* incoming light, we clearly identify the five distinguishable Fe 3*d* orbital states in the conduction band and the energy distribution of the Fe 3*d* orbital states is $d_{3z^2-r^2} > d_{x^2-y^2} > d_{zx} > d_{yz} > d_{xy}$, demonstrating that the Fe ions in the highly strained *T*-BFO are in the asymmetric $FeO_5$ pyramid. Therefore, a large spin canting angle is likely to be induced by the asymmetric $FeO_5$ pyramid, and further leads to a magnetic moment in the 17-nm-thick BFO thin films. The schematic diagram of the magnetic moment in the 17-nm-thick BFO thin films is shown in Fig. 6. Since the positions of the Fe ions are different, the orientation of the magnetic moment might be along the $[1\bar{1}0]$ or $[\bar{1}10]$ orientation [7]. For the highly strained *T*-BFO with the same ordered structural arrangement, the vector sum of the magnetic vector is parallel to the out-of-plane direction, which leads to the out-of-plane net magnetic moment. At the interface of two highly strained *T*-BFO unit cells with the different ordered structural arrangement, the magnetic moment vector sum generates in-plane and out-of-plane magnetic moment components. Therefore, an obvious magnetic moment should be observed in the 17-nm-thick BFO thin films.

With the increase of the BFO thin film thickness, the polarization-dependent O *K* edge XAS spectra obviously change. In Fig. 5(c), the Fe 3*d* orbital states are four

levels, and the energy distribution of the Fe 3*d* orbital states is $d_{x^2-y^2} > d_{3z^2-r^2} > d_{yz,zx} > d_{xy}$. This evident variation of the Fe 3*d* orbital states is derived from the Fe ions shifting, compared with the result of the 17-nm-thick BFO thin films. In the 43-nm-thick BFO thin films, the Fe ions shift to the center axis from the upper-right position in $FeO_5$ pyramid, as shown in Fig. 5(a). These results are consistent with that in previous report [34]. With the increase of the film thickness, the energy distribution of the Fe 3*d* orbital states in the 85-nm-thick BFO thin films is almost unchanged. According to the XRD and AFM data, the *T*-BFO, the $M_{C,tilt}$ and $S'_{tilt}$ exist in the 85-nm-thick BFO thin film surface. In the $S'_{tilt}$, the *c*-axis lattice parameter decreases and the Fe ions shift largely along the *c*-axis, causing the decrease of the Coulombic force between the Fe ion and neighboring O ions along the *c*-axis. Furthermore, the energy of the $d_{yz,zx}$ orbital state decreases. Since the *T*-BFO, the $M_{C,tilt}$ and the $S'_{tilt}$ exist in the 85-nm-thick BFO thin film surface, the $d_{yz,zx}$ orbital state should show two peaks (~529.5 eV for the *T*-BFO and the $M_{C,tilt}$, lower energy <529.5 eV for the $S'_{tilt}$) in the O *K* edge XAS spectra with the *E*//*c* incoming light. However, these two peaks don't appear in Fig. 5(d). So it indicates the existence of orbital reconstruction between the $M_{C,tilt}$ and the $S'_{tilt}$. When the thickness of the BFO layer reaches 170 nm, the energy distribution of the Fe 3*d* orbital states hardly change. Combined with the XRD and AFM data, the *R*-BFO, the $S'_{tilt}$, the $M_{C,tilt}$ and the *T*-BFO exist in the sample surface. In the *R*-BFO, the XAS spectra with the different incoming light polarizations (*E*//*c* and *E*//*a*) are almost the same and show two peaks. One peak represents the $d_{x^2-y^2}$ and $d_{3z^2-r^2}$ orbital states around 531 eV,

and another peak represents the $d_{xy}$, $d_{yz}$ and $d_{zx}$ orbital states around 530 eV [34]. But the characterized peaks of the *R*-BFO don't appear at ~530 eV in the XAS spectra with the *E*//*c* incoming light. This phenomenon indicates the existence of orbital reconstruction between the *R*-BFO and the $S'_{tilt}$. Since the orbital reconstruction can induce the strong magnetic coupling [36], the magnetic order of the $M_{C,tilt}$ and the $S'_{tilt}$ (or the $S'_{tilt}$ and the *R*-BFO) will be coupled with each other. Furthermore, it leads to a variation of the magnetic order at the phase boundaries or in the BFO phases.

## *3.3 Magnetic characterization*

To confirm the existence of the magnetic moment and analyze the magnetic property near the BFO phase boundaries, the *M–H* curves for the BFO thin films with different thicknesses at 300 K were performed, as shown in Fig. 7(a). For the 17-nm-thick BFO thin films, the significant magnetic signal is observed in the *M–H* curve. And the calculated average saturation magnetization is $(1.8\pm0.3)*10^5$ A/m. In Fig. 7(b), an obvious unsaturation magnetization at low temperatures (below 50 K) is observed. Due to the $T_N$=643 K, the unsaturation magnetization at low temperatures doesn't result from the paramagnetic contribution of the BFO. With the increase of the temperature, the magnetization can reach saturation at 6 T, demonstrating that the magnetic moment might be related to the spin canting. Moreover, in Figs. 7(c) and 7(d), the clear splitting in the ZFC-FC curves and the obvious XMCD signal in the XMCD spectra also reveal the existence of the net magnetic moment in the 17-nm-thick BFO thin films [37].

Previously, Ramesh *et al*. reported that a large saturation magnetization (~1.5*$10^5$ A/m) was in the *R*-BFO(70 nm)/$SrTiO_3$ and the saturation magnetization decreased with the increasing of the thickness. It indicated that the magnetic moment in the *R*-BFO thin films was related to the epitaxial strain [38]. In 2005, Eerenstein *et al*. demonstrated that the magnetic moment could be induced by the $Fe^{2+}$ [39]. Then, Remash *et al*. confirmed that the magnetic moment might be related to the enhanced canting angle, which could result from the epitaxial strain, oxygen vacancies or both [40]. In 2011, Ramesh *et al*. reported that the highly distorted *R*-BFO in the mixed phase BFO films had an enhanced saturation magnetization (~4.5*$10^4$ A/m), which arose from a piezomagnetic effect [41]. Therefore, although the view that the enhanced magnetic moment in the BFO thin films can be induced by the epitaxial strain is controversial, many experimental results demonstrate that the epitaxial strain can enhance the magnetic moment in the BFO thin films [42–44]. In this work, the saturation magnetization (1.8±0.3)*$10^5$ A/m in the 17-nm-thick BFO thin films was measured by the SQUID. Since the SQUID is a macroscopic measurement and it detects the total magnetic signal of the sample, the magnetic moment mainly results from the canted magnetic moment induced by the strain and the additional magnetic moment induced by the structure disorder and defects. With the increase of the thickness, the saturation magnetization decreases from 1.8*$10^5$ A/m to 1.3*$10^4$ A/m, as shown in Fig. 7(a). It is related to the phase transformation and the decrease of the spin canting angle, which is induced by the relaxation of the compressive strain. The BFO phases in the 43-nm-thick BFO thin films consist of the highly stained *T*-BFO

and the *T*-BFO phases. Previous work has shown that there is no magnetic signal in the *T*-BFO phase [41]. Moreover, the spin canting angle decreases in the highly stained *T*-BFO phase due to the relaxation of the compressive strain. Thus, the saturation magnetization in the 43-nm-thick BFO thin films obviously decreases, compared to that in the 17-nm-thick BFO thin films. The BFO phases in the 85-nm-thick BFO thin film are the highly strained *T*-BFO, the *T*-BFO, the $M_{C,tilt}$ and the $S'_{tilt}$ phases. According to the O *K* edge polarization-dependent XAS spectra, the orbital reconstruction exists between the $M_{C,tilt}$ and the $S'_{tilt}$ phases. The magnetic order changes at the $M_{C,tilt}/S'_{tilt}$ boundary or in the $M_{C,tilt}$ (or the $S'_{tilt}$) phase, leading to the enhanced saturation magnetization in the 85- and 128-nm-thick BFO thin films. The BFO phases at the 170-nm-thick BFO thin film are the highly *T*-BFO, the *T*-BFO, the $M_{C,tilt}$, the $S'_{tilt}$ and the *R*-BFO phases. In the *R*-BFO phase, a weak magnetic moment is induced by the structural distortions [8], and the magnitude of the magnetic moment is less than that of the $S'_{tilt}$ [25, 30, 41]. So the saturation magnetization decreases in the 170-nm-thick BFO thin films. Since the BFO phase compositions in the 85-nm-thick BFO thin films are complex, the magnetic properties at the $M_{C,tilt}/S'_{tilt}$ boundary or in the $M_{C,tilt}$ (or the $S'_{tilt}$) phase will still need to be investigated in future.

## 4. Conclusion

To summarize, we fabricated the 17-, 43-, 85-, 128-, 170-nm-thick BFO thin films on the LAO substrates by magnetron sputtering. In the 17-nm-thick BFO thin films, the phenomena that the [100] and [010] orientations of the BFO are parallel to

the [100] orientation of the LAO were observed by TEM. The polarization-dependent O *K* edge XAS spectra demonstrate the presence of the asymmetric $FeO_5$ pyramid, which causes the spin canting. And the spin canting can induce the magnetic moment. Thus, the magnetic signal in the 17-nm-thick BFO thin films was observed by the SQUID. Moreover, the in-plane structure disorder and defects might cause additional magnetic moment. For $t \geq 43$ nm, the polarization-dependent O *K* edge XAS spectra demonstrate that the orbital reconstruction at the interface between the $M_{C,tilt}/S'_{tilt}$ boundary or (the $S'_{tilt}/R$-BFO boundary), further leading to the variation of the magnetic order.

## Author Contribution Statement

**Zheng Wanchao:** Conceptualization, Methodology, Validation, Investigation, Resources, Formal analysis, Writing - Original Draft, Visualization. **Zheng Dongxing:** Investigation, Writing - Original Draft, Funding acquisition. **Li Dong:** Investigation, Writing - Review & Editing. **Li Peng:** Investigation, Writing - Review & Editing. **Zhang Linxing:** Investigation, Writing - Review & Editing. **Gong Junlu:** Writing - Review & Editing. **Pang Xin:** Writing - Review & Editing. **Jin Chao:** Writing - Original Draft. **Zhang Xixiang:** Writing - Review & Editing, Funding acquisition. **Bai Haili:** Writing - Original Draft, Funding acquisition.

## Acknowledgements

H.L.B. was supported by the National Natural Science Foundation of China (51772207 & 11434006). D.X.Z. was supported by the National Natural Science Foundation of China (11704278). P.L. and X.X.Z. acknowledge the financial support from King Abdullah University of Science and Technology (KAUST), Office of Sponsored Research (OSR) under the Award No. CRF-2015-SENSORS-2709 (KAUST). The authors acknowledge Professor Huanhua Wang and Associate Professor Yu Chen for valuable discussions. The authors acknowledge the Beijing Synchrotron Radiation Facility (1W1A and 4B9B beamlines, China), Shanghai Synchrotron Radiation Facility (08U1A beamline, China) and the National Synchrotron Radiation Laboratory (12B-a beamline, China) of the Chinese Academy of Sciences.

## References

[1] N. A. Hill, Why are there so few magnetic ferroelectrics?, J. Phys. Chem. B 104 (2000) 6694–6709. https://doi.org/10.1021/jp000114x.

[2] G. A. Smolenskiĭ and I. E. Chupis, Ferroelectromagnets, Sov. Phys. Usp. 25 (1982) 475–493. https://doi.org/10.3367/UFNr.0137.198207b.0415.

[3] V. E. Wood and A. Austin, Possible applications for magnetoelectric materials, Int. J. Magn 5 (1974) 303–315.

[4] I. Žutić, J. Fabian and S. D. Sarma, Spintronics: fundamentals and applications, Rev. Mod. Phys. 76 (2004) 323–410. https://doi.org/10.1103/RevModPhys.76.323.

[5] M. Fiebig, Revival of the magnetoelectric effect, J. Phys. D: Appl. Phys. 38 (2005) R123. https://doi.org/10.1088/0022-3727/38/8/r01.

[6] C. Binek and B. Doudin, Magnetoelectronics with magnetoelectrics, J. Phys.: Condens. Matter 17 (2004) L39. https://doi.org/10.1088/0953-8984/17/2/L06.

[7] G. J. MacDougall, H. M. Christen, W. Siemons, M. D. Biegalski, J. L. Zarestky, S. Liang, E. Dagotto and S. E. Nagler, Antiferromagnetic transitions in tetragonal-like $BiFeO_3$, Phys. Rev. B 85 (2012) 100406. https://doi.org/10.1103/PhysRevB.85.100406.

[8] C. Ederer and N. A. Spaldin, Weak ferromagnetism and magnetoelectric coupling in bismuth ferrite, Phys. Rev. B 71 (2005) 060401. https://doi.org/10.1103/PhysRevB.71.060401.

[9] J. H. Lee, K. Chu, A. A. Ünal, S. Valencia, F. Kronast, S. Kowarik, J. Seidel and C. H. Yang, Phase separation and electrical switching between two isosymmetric multiferroic phases in tensile strained $BiFeO_3$ thin films, Phys. Rev. B 89 (2014) 140101.

https://doi.org/10.1103/PhysRevB.89.140101.

[10] Z. Chen, Y. Qi, L. You, P. Yang, C. W. Huang, J. Wang, T. Sritharan and L. Chen, Large tensile-strain-induced monoclinic $M_B$ phase in $BiFeO_3$ epitaxial thin films on a $PrScO_3$ substrate, Phys. Rev. B 88 (2013) 054114. https://doi.org/10.1103/PhysRevB.88.054114.

[11] J. C. Yang, Q. He, S. J. Suresha, C. Y. Kuo, C. Y. Peng, R. C. Haislmaier, M. A. Motyka, G. Sheng, C. Adamo, H. J. Lin, Z. Hu, L. Chang, L. H. Tjeng, E. Arenholz, N. J. Podraza, M. Bernhagen, R. Uecker, D. G. Schlom, V. Gopalan, L. Q. Chen, C. T. Chen, R. Ramesh and Y. H. Chu, Orthorhombic $BiFeO_3$, Phys. Rev. Lett. 109 (2012) 247606. https://doi.org/10.1103/PhysRevLett.109.247606.

[12] H. M. Christen, J. H. Nam, H. S. Kim, A. J. Hatt and N. A. Spaldin, Stress-induced $R{-}M_A{-}M_C{-}T$ symmetry changes in $BiFeO_3$ films, Phys. Rev. B 83 (2011) 144107. https://doi.org/10.1103/PhysRevB.83.144107.

[13] H. Toupet, F. Le Marrec, C. Lichtensteiger, B. Dkhil and M. G. Karkut, Evidence for a first-order transition from monoclinic $\alpha$ to monoclinic $\beta$ phase in $BiFeO_3$ thin films, Phys. Rev. B 81 (2010) 140101. https://doi.org/10.1103/PhysRevB.81.140101.

[14] D. Mazumdar, V. Shelke, M. Iliev, S. Jesse, A. Kumar, S. V. Kalinin, A. P. Baddorf and A. Gupta, Nanoscale switching characteristics of nearly tetragonal $BiFeO_3$ thin films, Nano. Lett. 10 (2010) 2555–2561.

https://doi.org/10.1021/nl101187a.

[15] H. Liu, K. Yao, P. Yang, Y. Du, Q. He, Y. Gu, X. Li, S. Wang, X. Zhou and J. Wang, Thickness-dependent twinning evolution and ferroelectric behavior of epitaxial $BiFeO_3$ (001) thin films, Phys. Rev. B 82 (2010) 064108. https://doi.org/10.1103/PhysRevB.82.064108.

[16] R. J. Zeches, M. D. Rossell, J. X. Zhang, A. J. Hatt, Q. He, C. H. Yang, A. Kumar, C. H. Wang, A. Melville, C. Adamo, G. Sheng, Y. H. Chu, J. F. Ihlefeld, R. Erni, C. Ederer, V. Gopalan, L. Q. Chen, D. G. Schlom, N. A. Spaldin, L. W. Martin and R. Ramesh, A strain-driven morphotropic phase boundary in $BiFeO_3$, Science 326 (2009) 977–980. https://doi.org/10.1126/science.1177046.

[17] H. Béa, B. Dupé, S. Fusil, R. Mattana, E. Jacquet, B. Warot-Fonrose, F. Wilhelm, A. Rogalev, S. Petit, V. Cros, A. Anane, F. Petroff, K. Bouzehouane, G. Geneste, B. Dkhil, S. Lisenkov, I. Ponomareva, L. Bellaiche, M. Bibes and A. Barthélémy, Evidence for room-temperature multiferroicity in a compound with a giant axial ratio, Phys. Rev. Lett. 102 (2009) 217603. https://doi.org/10.1103/PhysRevLett.102.217603.

[18] D. Sando, A. Agbelele, D. Rahmedov, J. Liu, P. Rovillain, C. Toulouse, I. C. Infante, A. P. Pyatakov, S. Fusil, E. Jacquet, C. Carrétéro, C. Deranlot, S. Lisenkov, D. Wang, J. M. Le Breton, M. Cazayous, A. Sacuto, J. Juraszek, A. K. Zvezdin, L. Bellaiche, B. Dkhil, A. Barthélémy and M. Bibes, Crafting the magnonic and spintronic response of $BiFeO_3$ films by epitaxial strain, Nat.

Mater. 12 (2013) 641–646.

https://doi.org/10.1038/nmat3629.

[19] M. D. Rossell, R. Erni, M. P. Prange, J. C. Idrobo, W. Luo, R. J. Zeches, S. T. Pantelides and R. Ramesh, Atomic structure of highly strained $BiFeO_3$ thin films, Phys. Rev. Lett. 108 (2012) 047601.

https://doi.org/10.1103/PhysRevLett.108.047601.

[20] J. X. Zhang, Q. He, M. Trassin, W. Luo, D. Yi, M. D. Rossell, P. Yu, L. You, C. H. Wang, C. Y. Kuo, J. T. Heron, Z. Hu, R. J. Zeches, H. J. Lin, A. Tanaka, C. T. Chen, L. H. Tjeng, Y. H. Chu and R. Ramesh, Microscopic origin of the giant ferroelectric polarization in tetragonal-like $BiFeO_3$, Phys. Rev. Lett. 107 (2011) 147602.

https://doi.org/10.1103/PhysRevLett.107.147602.

[21] J. Li, J. Wang, M. Wuttig, R. Ramesh, N. Wang, B. Ruette, A. P. Pyatakov, A. K. Zvezdin and D. Viehland, Dramatically enhanced polarization in (001), (101), and (111) $BiFeO_3$ thin films due to epitiaxial-induced transitions, Appl. Phys. Lett. 84 (2004) 5261–5263.

https://doi.org/10.1063/1.1764944.

[22] P. S. Sankara Rama Krishnan, A. N. Morozovska, E. A. Eliseev, Q. M. Ramasse, D. Kepaptsoglou, W. I. Liang, Y. H. Chu, P. Munroe and V. Nagarajan, Misfit strain driven cation inter-diffusion across an epitaxial multiferroic thin film Interface, J. Appl. Phys. 115 (2014) 054103.

https://doi.org/10.1063/1.4862556.

[23] S. Nakashima, T. Uchida, K. Doi, K. Saitoh, H. Fujisawa, O. Sakata, Y. Katsuya, N. Tanaka and M. Shimizu, Strain evolution of epitaxial tetragonal-like $BiFeO_3$ thin films on $LaAlO_3$ (001) substrates prepared by sputtering and their bulk photovoltaic effect, Jpn. J. Appl. Phys. 55 (2016) 101501. https://doi.org/10.7567/JJAP.55.101501.

[24] Z. Chen, Z. Luo, C. Huang, Y. Qi, P. Yang, L. You, C. Hu, T. Wu, J. Wang, C. Gao, T. Sritharan and L. Chen, Low-symmetry monoclinic phases and polarization rotation path mediated by epitaxial strain in multiferroic $BiFeO_3$ thin films, Adv. Funct. Mater. 21 (2011) 133–138. https://doi.org/10.1002/adfm.201001867.

[25] A. R. Damodaran, C. W. Liang, Q. He, C. Y. Peng, L. Chang, Y. H. Chu and L. W. Martin, Nanoscale structure and mechanism for enhanced electromechanical response of highly strained $BiFeO_3$ thin films, Adv. Mater. 23 (2011) 3170–3175. https://doi.org/10.1002/adma.201101164.

[26] H. Dixit, C. Beekman, C. M. Schlepütz, W. Siemons, Y. Yang, N. Senabulya, R. Clarke, M. Chi, H. M. Christen and V. R. Cooper, Understanding strain-induced phase transformations in $BiFeO_3$ thin films, Adv. Sci. 2 (2015) 1500041. https://doi.org/10.1002/advs.201500041.

[27] J. Kreisel, P. Jadhav, O. Chaix-Pluchery, M. Varela, N. Dix, F. Sánchez and J. Fontcuberta, A phase transition close to room temperature in $BiFeO_3$ thin films, J. Phys.: Condens. Matter 23 (2011) 342202. https://doi.org/10.1088/0953-8984/23/34/342202.

[28] H. J. Liu, C. W. Liang, W. I. Liang, H. J. Chen, J. C. Yang, C. Y. Peng, G. F. Wang, F. N. Chu, Y. C. Chen, H. Y. Lee, L. Chang, S. J. Lin and Y. H. Chu, Strain-driven phase boundaries in $BiFeO_3$ thin films studied by atomic force microscopy and X-ray diffraction, Phys. Rev. B 85 (2012) 014104. https://doi.org/10.1103/PhysRevB.85.014104.

[29] D. Sando, B. Xu, L. Bellaiche and V. Nagarajan, A multiferroic on the brink: uncovering the nuances of strain-induced transitions in $BiFeO_3$, Appl. Phys. Rev. 3 (2016) 011106. http://dx.doi.org/10.1063/1.4944558.

[30] C. Beekman, W. Siemons, T. Z. Ward, M. Chi, J. Howe, M. D. Biegalski, N. Balke, P. Maksymovych, A. K. Farrar, J. B. Romero, P. Gao, X. Q. Pan, D. A. Tenne and H. M. Christen, Phase transitions, phase coexistence, and piezoelectric switching behavior in highly strained $BiFeO_3$ films, Adv. Mater. 25 (2013) 5561–5567. http://dx.doi.org/10.1002/adma.201302066.

[31] V. R. Singh, V. K. Verma, K. Ishigami, G. Shibata, Y. Yamazaki, A. Fujimori, Y. Takeda, T. Okane, Y. Saitoh, H. Yamagami, Y. Nakamura, M. Azuma and Y. Shimakawa, Enhanced ferromagnetic moment in Co-doped $BiFeO_3$ thin films studied by soft X-ray circular dichroism, J. Appl. Phys. 114 (2013) 103905. http://dx.doi.org/10.1063/1.4821024.

[32] J. M. D. Coey, Noncollinear spin arrangement in ultrafine ferrimagnetic crystallites, Phys. Rev. Lett. 27 (1971) 1140–1142.

https://doi.org/10.1103/PhysRevLett.27.1140.

[33] H. Béa, M. Bibes, S. Fusil, K. Bouzehouane, E. Jacquet, K. Rode, P. Bencok and A. Barthélémy, Investigation on the origin of the magnetic moment of $BiFeO_3$ thin films by advanced X-ray characterizations, Phys. Rev. B 74 (2006) 020101. https://doi.org/10.1103/PhysRevB.74.020101.

[34] K. T. Ko, M. H. Jung, Q. He, J. H. Lee, C. S. Woo, K. Chu, J. Seidel, B. G. Jeon, Y. S. Oh, K. H. Kim, W. I. Liang, H. J. Chen, Y. H. Chu, Y. H. Jeong, R. Ramesh, J. H. Park and C. H. Yang, Concurrent transition of ferroelectric and magnetic ordering near room temperature, Nat. Commun. 2 (2011) 567. https://doi.org/10.1038/ncomms1576.

[35] K. I. Kugel' and D. I. Khomskiĭ, The Jahn-Teller effect and magnetism transition metal compounds, Sov. Phys. Usp. 25 (1982) 231–256. https://doi.org/10.1070/PU1982v025n04ABEH004537.

[36] P. Yu, J. S. Lee, S. Okamoto, M. D. Rossell, M. Huijben, C. H. Yang, Q. He, J. X. Zhang, S. Y. Yang, M. J. Lee, Q. M. Ramasse, R. Erni, Y. H. Chu, D. A. Arena, C. C. Kao, L. W. Martin and R. Ramesh, Interface ferromagnetism and orbital reconstruction in $BiFeO_3$-$La_{0.7}Sr_{0.3}MnO_3$ heterostructures, Phys. Rev. Lett. 105 (2010) 027201. https://doi.org/10.1103/PhysRevLett.105.027201.

[37] X. Marti, V. Skumryev, C. Ferrater, M. García-Cuenca, M. Varela, F. Sánchez and J. Fontcuberta, Emergence of ferromagnetism in antiferromagnetic $TbMnO_3$ by epitaxial strain, Appl. Phys. Lett. 96 (2010) 222505.

https://doi.org/10.1063/1.3443714.

[38] J. Wang, J. B. Neaton, H. Zheng, V. Nagarajan, S. B. Ogale, B. Liu, D. Viehland, V. Vaithyanathan, D. G. Schlom, U. V. Waghmare, N. A. Spaldin, K. M. Rabe, M. Wuttig and R. Ramesh, Epitaxial $BiFeO_3$ multiferroic thin film heterostructures, Science 299 (2003) 1719–1722.

https://doi.org/10.1126/science.1080615.

[39] W. Eerenstein, F. D. Morrison, J. Dho, M. G. Blamire, J. F. Scott and N. D. Mathur, Comment on "epitaxial $BiFeO_3$ multiferroic thin film heterostructures", Science 307 (2005) 1203a.

https://doi.org/10.1126/science.1105422.

[40] J. Wang, A. Scholl, H. Zheng, S. B. Ogale, D. Viehland, D. G. Schlom, N. A. Spaldin, K. M. Rabe, M. Wuttig, L. Mohaddes, J. Neaton, U. V. Waghmare, T. Zhao and R. Ramesh, Response to comment on ‘‘epitaxial $BiFeO_3$ multiferroic thin film heterostructures’’, Science 307 (2005) 1203b.

https://doi.org/10.1126/science.1103959.

[41] Q. He, Y. H. Chu, J. T. Heron, S. Y. Yang, W. I. Liang, C. Y. Kuo, H. J. Lin, P. Yu, C. W. Liang, R. J. Zeches, W. C. Kuo, J. Y. Juang, C. T. Chen, E. Arenholz, A. Scholl and R. Ramesh, Electrically controllable spontaneous magnetism in nanoscale mixed phase multiferroics, Nat. Commun. 2 (2011) 225.

https://doi.org/10.1038/ncomms1221.

[42] C.-J. Cheng, C. Lu, Z. Chen, L. You, L. Chen, J. Wang and T. Wu, Thickness-dependent magnetism and spin-glass behaviors in compressively

strained $BiFeO_3$ thin films, Appl. Phys. Lett. 98 (2011) 242502. https://doi.org/10.1063/1.3600064.

[43] S. Ryu, J.-Y. Kim, Y.-H. Shin, B.-G. Park, J. Y. Son and H. M. Jang, Enhanced magnetization and modulated orbital hybridization in epitaxially constrained $BiFeO_3$ thin films with rhombohedral symmetry, Chem. Mater. 21 (2009) 5050–5057. https://doi.org/10.1021/cm9014496.

[44] J. Wu, G. Kang, H. Liu and J. Wang, Ferromagnetic, Ferroelectric, and fatigue behavior of (111)-oriented $BiFeO_3/(Bi_{1/2}Na_{1/2})TiO_3$ lead-free bilayered thin films, Appl. Phys. Lett. 94 (2009) 172906. https://doi.org/10.1063/1.3127519.

# Table

**Table 1** Lattice constants $a_{T\text{-BFO}}$, $b_{T\text{-BFO}}$, and $c_{T\text{-BFO}}$ for the $t$-nm-thick BFO thin films.

| $t$ (nm) | $a_{T\text{-BFO}}$ (nm) | $b_{T\text{-BFO}}$ (nm) | $c_{T\text{-BFO}}$ (nm) | $c_{T\text{-BFO}}/a_{T\text{-BFO}}$ |
|---|---|---|---|---|
| 17 | 0.382±0.002 | 0.379±0.002 | 0.454±0.001 | 1.19 |
| 85 | 0.381±0.002 | 0.375±0.002 | 0.465±0.001 | 1.22 |
| 170 | 0.384±0.002 | 0.375±0.002 | 0.466±0.001 | 1.21 |

## Figure captions

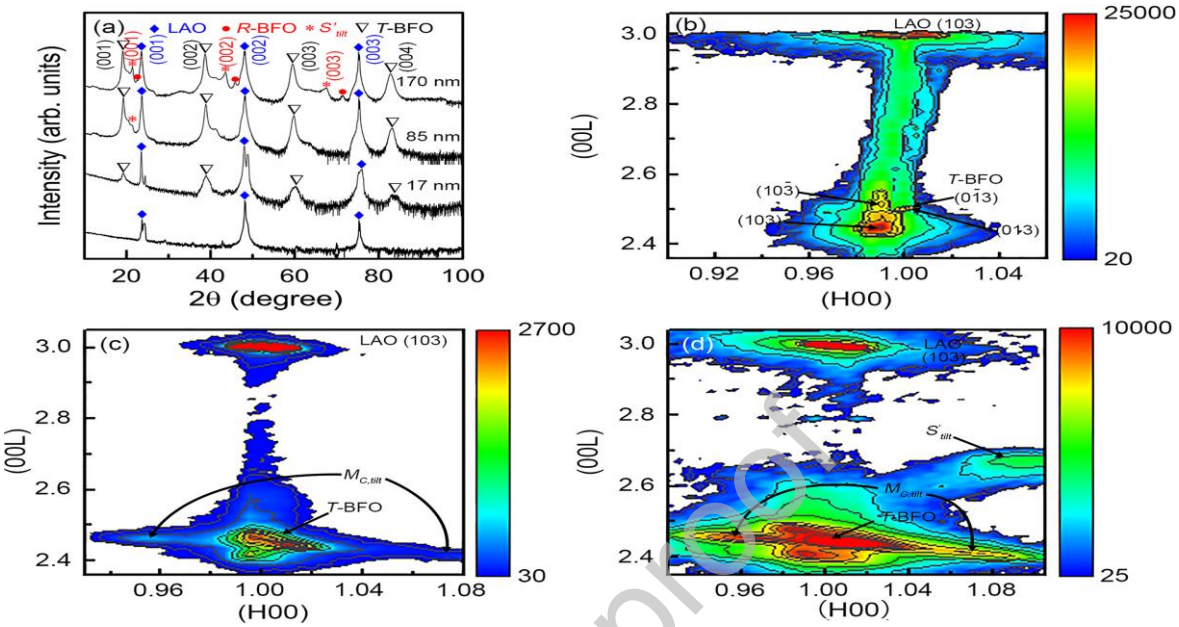


**Fig. 1** (a) XRD patterns of the 17-, 85-, 170-nm-thick BFO thin films and the LAO (001) substrate. RSM of the (103) reflection of (b) 17-, (c) 85-, and (d) 170-nm-thick BFO thin films.

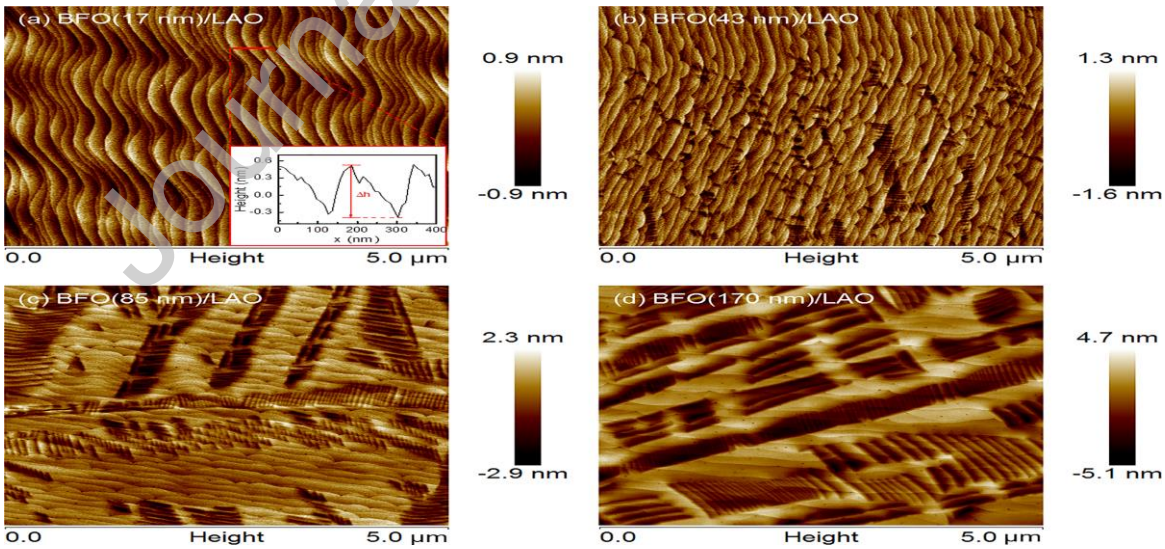


**Fig. 2** Surface morphologies of the (a) 17-, (b) 43-, (c) 85-, and (d) 170-nm-thick BFO thin films. The inset shows the height data of the labeled region.

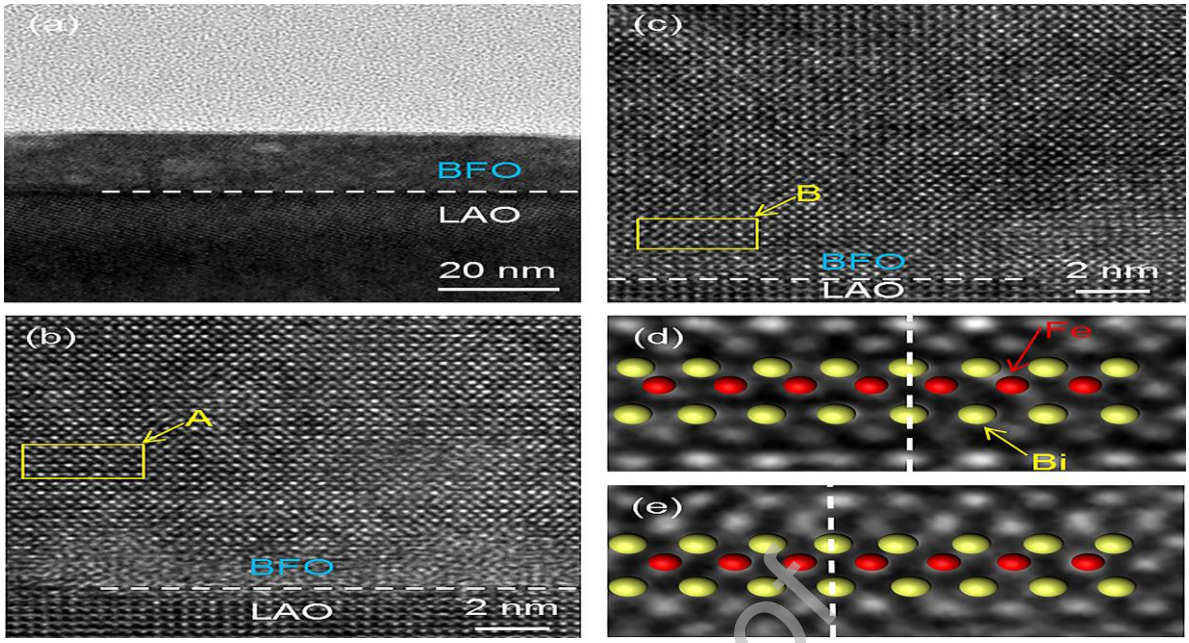


**Fig. 3** (a) TEM cross-sectional images at the BFO(17 nm)/LAO interface. (b) and (c) HRTEM images at the BFO(17 nm)/LAO interface. (d) and (e) Magnified patterns of the region A and region B respectively. The yellow ball is the Bi ion and the red ball is the Fe ion.

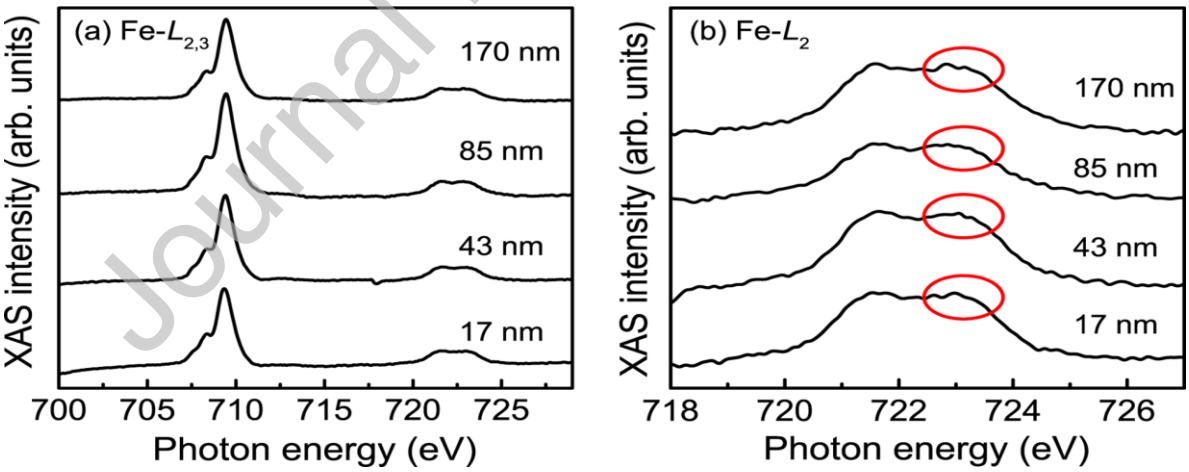


**Fig. 4** (a) XAS spectra at the Fe $L_{2,3}$ edge for the BFO thin films with different thicknesses. (b) Zoomed area of (a) next to the Fe $L_2$ edge for the BFO thin films.

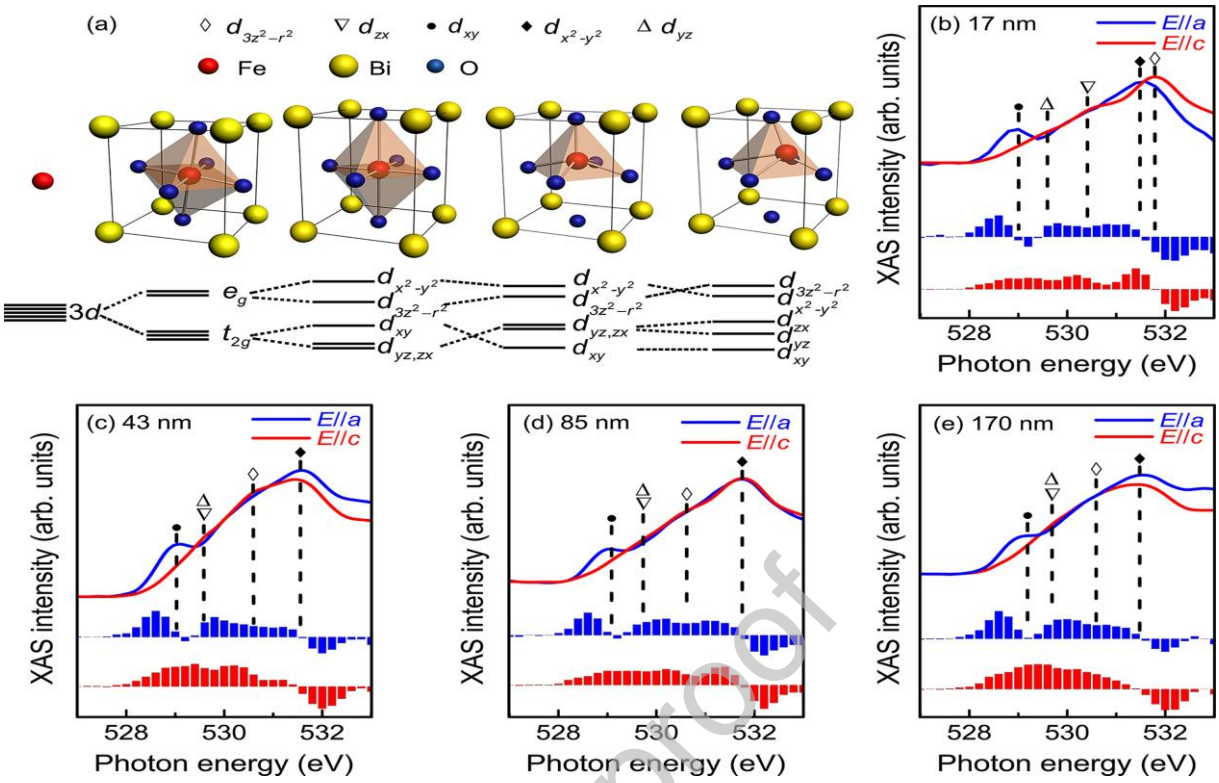


**Fig. 5** (a) Local structure of the transition metal oxide and the 3*d* level splits in different site symmetries. The ball represents different elements as follows: the red ball Fe ion, blue ball O ion, and yellow ball Bi ion. (b-e) Polarization-dependent XAS spectra at O *K* edge for the 17-, 43-, 85- and 170-nm-thick BFO thin films. The blue line represents the O *K* edge XAS with the *E*//*a* incoming light. The red line represents the O *K* edge XAS with the *E*//*c* incoming light. The histograms represent the slope of polarization-dependent XAS at O *K* edge [*E*//*a* (blue column) and *E*//*c* (red column)]. The black filled diamond represents the $d_{x^2-y^2}$ orbital state. The empty diamond represents the $d_{3z^2-r^2}$ orbital state. The empty lower triangle represents the $d_{zx}$ orbital state. The empty upper triangle represents the $d_{yz}$ orbital state. The black dot represents the $d_{xy}$ orbital state.

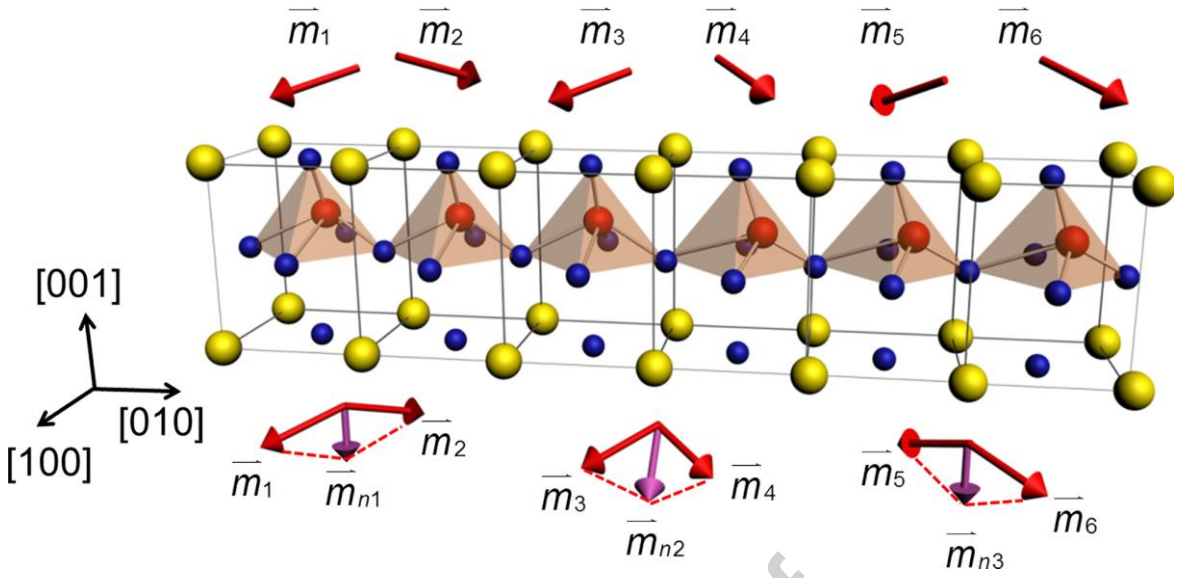


**Fig. 6** Schematic diagram of the magnetic moment in the 17-nm-thick BFO thin films (corresponding to the Fig. 3(e)), the $\vec{m}_1$, $\vec{m}_2$, $\vec{m}_3$, $\vec{m}_4$, $\vec{m}_5$ and $\vec{m}_6$ represent the magnetic vectors of the highly strained *T*-BFO, and the $\vec{m}_{n1}$, $\vec{m}_{n2}$ and $\vec{m}_{n3}$ are the vector sum of the magnetic vector.

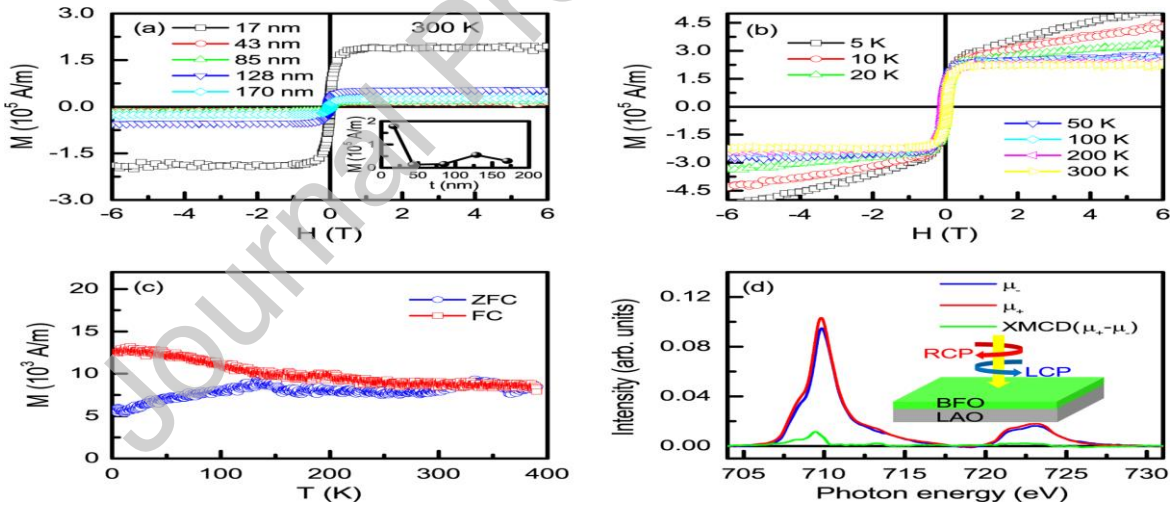


**Fig. 7** (a) *M–H* curves for the 17-, 43-, 85-, 128-, 170-nm-thick BFO thin films at 300 K. The inset shows the *M–t* curve. (b) *M–H* curves for the 17-nm-thick BFO thin films at different temperatures. (c) ZFC–FC curves of the 17-nm-thick BFO thin film after the subtraction of the LAO substrate response. The range of temperature is from 5 K to 390 K and the external magnetic field is 0.03 T. (d) Fe

$L_{2,3}$ edge XAS and XMCD spectra for the 17-nm-thick BFO thin films at room temperature. The blue line represents the Fe $L_{2,3}$ edge XAS ($\mu_-$) with the left circularly polarized (LCP) incoming light. The red line represents the Fe $L_{2,3}$ edge XAS ($\mu_+$) with the right circularly polarized (RCP) incoming light. The green line represents the Fe $L_{2,3}$ edge XMCD spectra, which is the difference value between the $\mu_-$ and the $\mu_+$.

**Declaration of interests**

☒ The authors declare that they have no known competing financial interests or personal relationships that could have appeared to influence the work reported in this paper.

☐The authors declare the following financial interests/personal relationships which may be considered as potential competing interests: